

3D Printed Materials with Nanovoxelated Elastic Moduli

Peter L. H. Newman,* Mohammad Mirkhalaf, Steven C. Gauci, Iman Roohani, Maté Biro, Christopher Barner-Kowollik, and Hala Zreiqat

Fabrication methods that synthesize materials with higher precision and complexity at ever smaller scales are rapidly developing. Despite such advances, generating complex 3D materials with controlled mechanical properties at the nanoscale remains challenging. Exerting precise control over mechanical properties at the nanoscale would enable material strengths near theoretical maxima, and the replication of natural structures with hitherto unattainable strength-to-weight ratios. Here, a method for fabricating materials with nanovoxelated elastic moduli by employing a volume-conserving photoresist composed of a copolymer hydrogel, along with OpenScribe, an open-source software that enables the precise programming of material mechanics, is presented. Combining these, a material composed of periodic unit cells featuring heteromechanically tessellated soft-stiff structures, achieving a mechanical transition over an order-of-magnitude change in elastic modulus within 770 nm, a 130-fold improvement on previous reports, is demonstrated. This work critically advances material design and opens new avenues for fabricating materials with specifically tailored properties and functionalities through unparalleled control over nanoscale mechanics.

as high strength and toughness,^[2–5] auxeticity,^[6–9] responsiveness to external stimuli,^[10–13] and the ability to compute.^[14,15] Among these methods, those achieving nanoscale resolution are uniquely desirable. At this scale, materials can be engineered to reach near-theoretically maximum strength due to mechanisms that minimize flaw sensitivity.^[16,17] Additionally, materials with rationally designed nanostructures can incorporate energy-absorbing mechanisms such as crack guiding, thereby enhancing resistance to deformation and failure under various stress conditions.^[18] Incorporating these mechanisms into multiscale hierarchies, starting at the nanoscale, has been shown to improve strength-to-weight ratios and toughness by more than two orders of magnitude, as observed in wood, nacre, and seashells.^[16–22]

3D printing has become a cornerstone technology for developing advanced materials with unique mechanical properties.

Both traditional single-material 3D printing^[23] and emerging multimaterial techniques^[24] allow precise specification of material compositions. Multimaterial 3D printing broadens the

1. Introduction

Precision^[1] fabrication methods are critical for developing advanced materials with exceptional mechanical properties such

P. L. H. Newman, H. Zreiqat
The School of Biomedical Engineering
The University of Sydney
Sydney, Australia
E-mail: peter.newman1@unsw.edu.au

P. L. H. Newman, M. Biro
EMBL Australia
Single Molecule Science node
School of Biomedical Sciences
University of New South Wales
Sydney, NSW 2052, Australia

M. Mirkhalaf
School of Mechanical
Medical and Process Engineering
Queensland University of Technology
2 George St, Brisbane, QLD 4000, Australia
S. C. Gauci, C. Barner-Kowollik
School of Chemistry and Physics
Centre for Materials Science
Queensland University of Technology (QUT)
2 George Street, Brisbane, QLD 4000, Australia

I. Roohani
School of Biomedical Engineering
Faculty of IT and Engineering
University of Technology Sydney
Sydney, NSW 2007, Australia

C. Barner-Kowollik
Institute of Nanotechnology (INT)
Karlsruhe Institute of Technology (KIT)
Hermann-von-Helmholts-Platz 1, 76344 Eggenstein-Leopoldshafen,
Germany

C. Barner-Kowollik
Institute of Functional Interfaces (IFG)
Karlsruhe Institute of Technology (KIT)
Hermann-von-Helmholts-Platz 1, 76344 Eggenstein-Leopoldshafen,
Germany

The ORCID identification number(s) for the author(s) of this article can be found under <https://doi.org/10.1002/adma.202416262>

© 2025 The Author(s). Advanced Materials published by Wiley-VCH GmbH. This is an open access article under the terms of the [Creative Commons Attribution-NonCommercial-NoDerivs](#) License, which permits use and distribution in any medium, provided the original work is properly cited, the use is non-commercial and no modifications or adaptations are made.

DOI: 10.1002/adma.202416262

material design space, facilitating the fabrication of materials with increasingly exotic properties. However, current multimaterial 3D printing faces limitations due to its reliance on a switching process, which has typically involved the use of a solid wiper,^[25] fluid flow,^[26,27] multiple extruders,^[24] or a mixing/valve system.^[28] The switching process can restrict build size, narrow the range of usable materials, reduce printing speeds, increase the risk of material contamination, and hinder functional interfaces and integration. Current technologies for multimaterial 3D printing, such as direct ink writing, extrusion, and polyjet printing – producing multimaterial structures with features at the millimeter^[29–33] or hundreds of microns scales,^[1,24,26] are too large to exploit the above-discussed benefits available to nanoscale structures. Although there have been prior efforts to fabricate heterogeneous nanostructures using 3D printing, those methods did not achieve precise control over the mechanical properties of the material at nanoscales.^[34–36]

Materials with nanovoxelated elastic moduli are those where the elastic properties can be precisely controlled within discrete volumetric elements (voxels) at the nanoscale (<1 μm), similar to how digital images are composed of pixels with distinct properties (Figure 1a). This concept is fundamental in modern 3D printing technologies, where objects are digitized before fabrication. Implicitly, objects are represented in a binary manner, where the printer's build space either contains – or does not contain – the object. This binary representation can be extended to define voxels of arbitrary material properties, thus defining complex material compositions. In our work, “nanovoxelated elastic moduli” refers to materials where these discrete volumes have independently controllable elastic properties at the nanoscale, with demonstrated transitions between different mechanical properties occurring over distances less than 1 μm.

Extending this binary representation to encompass voxels of varied elasticity, we introduce a novel fabrication technology for generating materials with nanovoxelated elasticity. This breakthrough is facilitated by the dual innovation of a non-swelling photoresist specifically designed for 3D nanoprinting using multiphoton lithography (Figure 1b; Figures S1, S2, Table S1, Supporting Information), alongside a custom software tool named OpenScribe (Figure 1c; Figures S3, S4, Table S2, Supporting Information). The photoresist enables the stable fabrication of nanostructures with precisely tunable elastic moduli, addressing challenges associated with swelling and structural integrity at the nanoscale. Concurrently, OpenScribe provides a platform for designing and voxelating complex material architectures, allowing for the precise control of spatially varying mechanical properties within a printed object.

Building upon this concept, we introduce a fabrication method able to generate materials that are elastically heterogeneous with nanoscale precision. This breakthrough is facilitated by our development and optimization of two key components, 1) a novel non-swelling photoresist specifically designed for rapid multiphoton lithography, and 2) an open-source software tool named OpenScribe. The photoresist allows for the generation of stable nanostructures with precisely tunable elastic moduli, preventing the common failure mode where differential swelling between adjacent materials regions of differing properties generates internal stresses that delaminate constituent materials and compromise structural integrity. The OpenScribe software com-

plements our photoresist by providing a platform for the precision design of material properties in complex voxelated material architectures, granting unprecedented control over spatially varying mechanical properties at the nanoscale. Together, these innovations surmount the limitations of current multimaterial 3D printing technologies, enabling the production of materials with programmable elasticity and nanoscale feature resolution. Our work not only represents a significant advancement in additive manufacturing, but also opens new avenues for engineering materials with tailored mechanical properties for advanced applications.

2. Results

To achieve materials with nanovoxelated elastic moduli, we develop a novel non-swelling photoresist for 3D nanoprinting (3DNP) with a multiphoton lithographic device (Nanoscribe Photonic Professional GT2) (Figure 1b; Figures S1, S2, Table S1, Supporting Information). Our photoresist is composed of a two-component copolymer hydrogel, allowing precise tuning of polymer properties through adjustments in the composition of the two polymer components. This approach enables us to achieve properties along a continuum between the two hydrophilic or hydrophobic prepolymers, resulting in a non-swelling polymer that remains stable without delamination or tearing after printing. Polymerization is initiated via photoinitiator phenylbis(2,4,6-trimethylbenzoyl)phosphine oxide (BAPO).^[37] Further enhancements to enable efficient printing include an enzymatic oxidase system comprising glucose and glucose oxidase^[38] (Figure 1b and Table S1, Supporting Information). This system actively removes dissolved oxygen through enzymatic consumption (glucose + O₂ → gluconic acid + H₂O₂), reducing oxygen's inhibitory effects on the polymerization reaction. In photopolymerization, oxygen typically acts as a radical scavenger, competitively reacting with both photoexcited initiator molecules and propagating polymer chains. By depleting oxygen, the glucose system enhances polymerization efficiency and enables complete cure at lower laser powers and exposure times.^[38] The photoresist also includes the thickener, hydroxypropyl-methyl cellulose, which increases viscosity and restricts molecular mobility. The viscosity enhancement serves multiple functions: limiting oxygen diffusion into the photoresist, controlling the spatial distribution of photoinitiated free radicals, and reducing radical termination through diffusion-limited collisions. Together, these mechanisms support rapid printing while maintaining high spatial resolution and reproducibility^[39] (refer to the Supporting Information for a detailed discussion on the constituents of the photoresist).

Further enhancements that ensure rapid printing include: an enzymatic oxidase system comprising G/GO, which acts to reduce oxidative inhibition of the polymerization reaction; the thickener hydroxypropyl-methyl cellulose, to increase the viscosity of the resist, which restricts the mobility of both inhibitory oxygen species, as well as photoinitiated free radicals – a known mechanism for regulating 3D printing – supporting high reproducibility and increased printing resolution (Figure 1b and Table S1, Supporting Information).

We aimed to develop a photoresist suitable for versatile applications, including those requiring immersion in water and specific biofunctionalities. We thus opted for a bioinert prepolymer

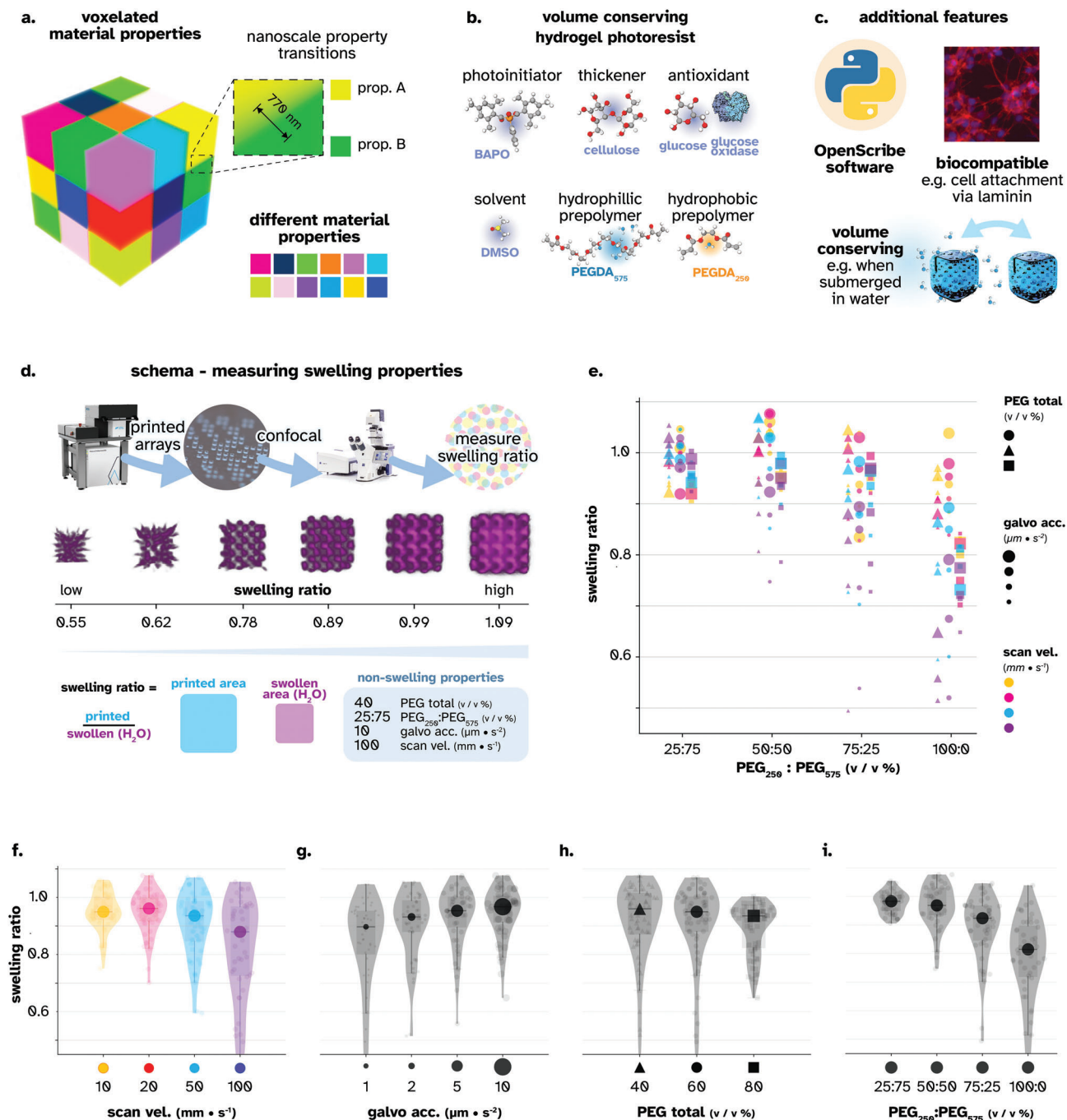


Figure 1. Voxelating material properties without structural deformation. a) A material with voxelated properties, wherein color represents voxels of arbitrary material properties – inset shows the transition between material properties b) A photoresist for 3D printing materials with nanovoxelated elastic modulus. The photoresist uses DMSO as a solvent for its high solvency, with hydroxypropyl-methyl cellulose to enhance viscosity, and an enzymatic oxidase system of glucose and glucose oxidase, reducing oxidative inhibition. Photopolymerization is initiated by the photoinitiator BAPO, polymerizing the hydrophilic (PEGDA₅₇₅) and hydrophobic (PEGDA₂₅₀) prepolymers. c) Additional developments include the OpenScribe software for defining objects with complex voxelated properties, and biocompatibility of the photoresist via the incorporation of biomolecules with free cysteine residues into the hydrogel. d) Workflow for measuring the swelling properties of the printed hydrogel: printed arrays are imaged using confocal microscopy to measure their swelling ratio, defined as their deviation from the ideal shape following water immersion. Example images show prints with swelling ratios ranging from 0.55 to 1.09. e) Swelling ratio as a function of PEGDA₅₇₅ to PEGDA₂₅₀ ratios. Different markers indicate varying total PEG concentrations (40%, 60%, 80%, 100%), galvo acceleration (1, 5, 10 $\mu\text{m} \cdot \text{s}^{-2}$), and scan velocities (10, 20, 50, 100 $\text{mm} \cdot \text{s}^{-1}$). Violin plots showing the distribution of swelling ratio data projected onto individual parameters, with overlaid box-plot showing mean, 1st/3rd quartile lines, and limits. Each plot represents a single-parameter projection of the multi-dimensional parameter space. f) scan velocity, g) galvo acceleration, h) total PEG concentration, and i) PEGDA₅₇₅ to PEGDA₂₅₀ ratio.

molecule over a biocompatible one, since specific biological functionalities could then be integrated through further additions. For example, laminin can be added to the photoresist at $50 \mu\text{g mL}^{-1}$ to dictate specific cell attachment characteristics, including the attachment of human pluripotent stem cells (Figure 1c; Figure S5, Supporting Information). Such biomolecules are covalently integrated into the hydrogel through thiol-ene conjugation between PEGDA and any free thiol groups present from cysteine residues.^[40]

We introduce OpenScribe, the first software tool designed specifically for creating materials with programmable elastic properties at the nanoscale (Figure 1c; Figure S2, Table S2, Supporting Information). OpenScribe introduces a new multi-material paradigm that enables precise control over mechanical properties throughout a nanoprinted structure. The software bridges the gap between design intent and fabrication by automatically translating desired elastic modulus values into optimized laser parameters while implementing sophisticated control algorithms that maintain consistent mechanical properties at the nanoscale. Key features include efficient handling of complex periodic structures, common in the design of next-generation metamaterials, by allowing users to select predefined mathematical structures such as gyroids and octet trusses, or upload custom unit cell designs via *.STL files – while maintaining practical file sizes. The software also introduces multi-object printing sequences, height-dependent laser power adjustment, and advanced field printing strategies, specification of illumination compensation functions to avoid uneven print fields due to local heating effects and radical diffusion. OpenScribe enables precise programming of nanoscale features and elastic moduli through either a scriptable environment or graphical user interface, with its Python codebase accessible across Windows, macOS, and Linux, encouraging collaborative advancements in material science, particularly in the design and fabrication of the next-generation of complex nanostructured materials. The capabilities of OpenScribe are detailed further in the Supplementary Information (Table S2, Supporting Information).

We hypothesized that achieving mechanical heterogeneity could be achieved by precisely varying the polymer density within the hydrogel. However, this approach led to a problem: hydrogels tend to swell in proportion to their polymer density. As a result, the changes intended to alter mechanical properties would cause increased swelling, internal strain, and material distortion or destruction.^[41] To address this, it was essential to develop a volume-conserving material – one in which the swelling ratio, or the relative change in volume following water immersion, was one (Figure 1d). Consequently, this would maintain structural integrity and avoid deformation, ensuring that stiffness variations did not compromise the printed material's mechanical stability.

We employed a block copolymer strategy using two different polyethylene glycol diacrylate (PEGDA) prepolymers with average molecular weights (M_n) of 250 and 575 (PEGDA250 and PEGDA575). While PEGDA575 is hydrophilic, PEGDA250 is hydrophobic, with their combined polymerization state affecting the overall hydrophilicity. To find optimal conditions for synthesizing a material with a swelling ratio of one, we quantified shape deviation from the ideal printed structure using confocal imaging following overnight submersion in water. We project the multiparametric dataset into 2D visualizations that highlight

key relationships. The relative (Figure 1e,i) and total amounts (Figure 1e,h) of the copolymer were assessed, finding increasing PEGDA250 relative to PEGDA575 decreased the swelling ratio, likely due to the increased hydrophobicity of the polymer (Figure 1e,h,i). This characterization was performed alongside adjustments to key printer settings that influence the light energy delivered to the photoresist during fabrication. These include the laser scan velocity (the speed at which the focused laser beam is scanned across the photoresist, measured in mm s^{-1}) and galvanometer acceleration (the rate at which the laser's scanning mirrors accelerate the laser beam to this target velocity, measured in $\mu\text{m s}^{-2}$). We found that modulating these parameters affected the swelling behavior of printed structures – with lower scan velocities or higher galvanometer acceleration increasing the swelling ratio (Figure 1f,g). This relationship likely stems from increased energy absorption at slower scanning speeds or during rapid mirror acceleration, leading to higher crosslinking density in the printed material.

Considering this multi-parameter data, one can determine the conditions that most stably produce prints with a swelling ratio of one by evaluating the gradient of the multiparametric fit. However, this approach suggests that longer print times are more desirable. Alternatively, by fixing the scan velocity at 100 mm s^{-1} , we optimized for both print speed and swelling ratio, finding that volumetric changes and material strains were sufficiently low to avoid delamination and other structural deformations. Therefore, we formulated a fast-curing, volume-conserving photoresist using a dimethyl sulfoxide (DMSO)-based composition with glucose (3.8%), glucose oxidase (0.23%), cellulose (2%), BAPO (65 mg mL^{-1} , Figure S6, Supporting Information) PEGDA250 (10%), and PEGDA575 (30%). The selected printer settings of $10 \mu\text{m s}^{-2}$ galvo acceleration and 100 mm s^{-1} scan velocity provided a compromise between print speed and volume conservation, ensuring the printed hydrogel maintained its shape, integrity, and mechanical properties post-printing.

To control the local elastic modulus of printed materials, we aimed to create localized regions of precisely defined polymeric density. We systematically varied printer-defined parameters (i.e., laser power and hatch volume) that alter the energy absorbed by the photoresist and quantitatively assessed the elastic moduli of the printed materials using AFM force spectroscopy (Figure 2a; Figure S7, Supporting Information). We hypothesized that increasing energy would enhance polymerization, thereby increasing both material density and the elastic modulus. To test this hypothesis, we studied how changes in laser power (Figure 2b,c) and hatch volume (Figure 2b,d), influenced the elasticity of printed materials. Hatch volume was calculated by squaring the distance between adjacent laser beam paths within the rasterization plane and multiplying by the distance between adjacent rasterization planes.

Our results showed that increasing the energy absorbed in a given volume—either through higher laser powers or a smaller hatching volume—resulted in higher elastic moduli (Figure 2; Figure S8, Supporting Information). This correlation between laser energy input and polymeric cross-linking density demonstrated a range of elastic moduli from 1.6 to 44 kPa. Fitting this data permitted the mapping of a given laser power and hatching volume with an elastic modulus, explored in depth below (Figure 3). These findings underscore our method's ability to

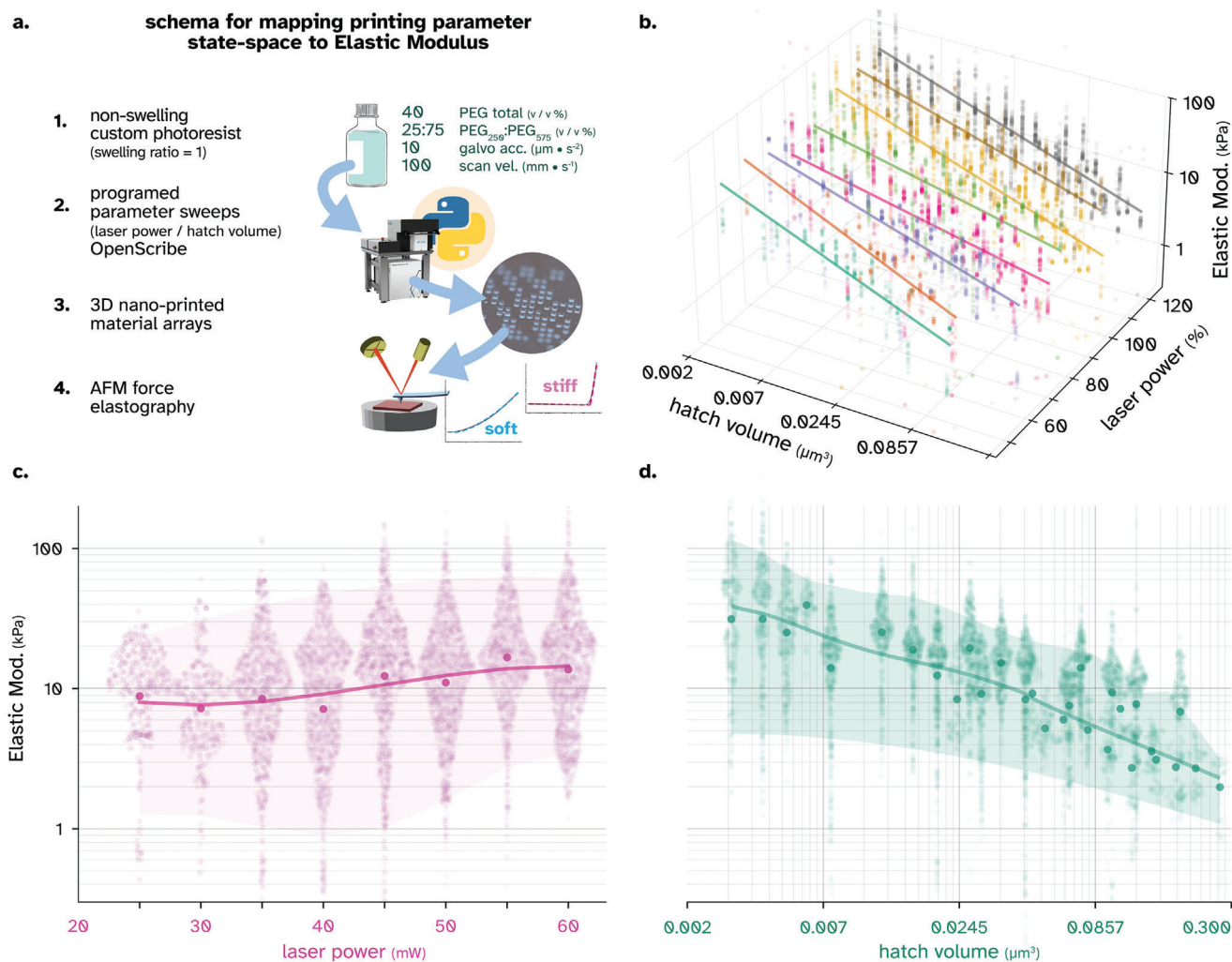


Figure 2. Relationship of print conditions with elastic modulus. a) Schematic representation of the experimental setup for printing large arrays with systematically varied properties. The custom photoresist with a swelling ratio of 1 was used. OpenScribe software was employed to program parameter variations, including laser power and hatch volume. The printed materials were then analyzed using atomic force microscopy (AFM) force spectroscopy to measure their elastic modulus. b) 3D plot showing the relationship between hatch volume, laser power, and elastic modulus, with an exponential fit (appearing linear due to semi-log y-axis). c) Violin plot depicting the effect of laser power on elastic modulus with cubic spline fit. d) Violin plot illustrating the impact of hatch volume on elastic modulus with cubic spline fit. Individual data points show all experimental replicates ($n = 16$ measurements per condition, repeated in triplicate), with splines-of-best-fit plotted to highlight trends. Violin plots show the distribution of measurements projected onto single parameters while holding other variables constant. For a complete unprojected dataset across all experimental parameters, see (Figure S8, Supporting Information).

finely tune mechanical properties through controlled print parameters, representing a significant advancement in the fabrication of nanoscale metamaterials, in turn permitting the design of materials with voxels of precisely specified elasticity via the OpenScribe software.

We next aimed to fabricate materials with precisely designed elasticity at nanoscale resolution. This was enabled by utilizing our volume-conserving photoresist together with the OpenScribe software (Figure 3a). Our demonstration focused on designs using a lattice-based periodic network, as these are ubiquitous in naturally occurring multiscale hierarchical materials and modern metamaterials.^[6,16,42] We selected various unit cell structures to demonstrate the heteromechanical properties of our system, printing periodic unit cells with distinct mechanical phases. This

included unit cell lattices of Weaire–Phelan (Figure 3), gyroid, cubic, octet truss, and Kelvin foam structures (Figures S10–S17, Supporting Information). These designs featured a stiff lattice region with an elastic modulus of 30 kPa tessellated by a soft region of 3 kPa. This approach resulted in monolithic composite heteromaterials, where each 50 μm cube was composed of 5 μm unit cells, amounting to 10 repeating units in each dimension. In the case of the Weaire–Phelan lattice, each 50 μm cube contained 5 repeating units of 10 μm cells, due to its unique structure composed of a combination of two distinct polyhedral cells, resulting in a different repetition pattern. For visualization and structural verification, we employed confocal microscopy, capitalizing on the autofluorescence of PEG when excited by ultra-violet light (Figure S10, Supporting Information). This property allowed us

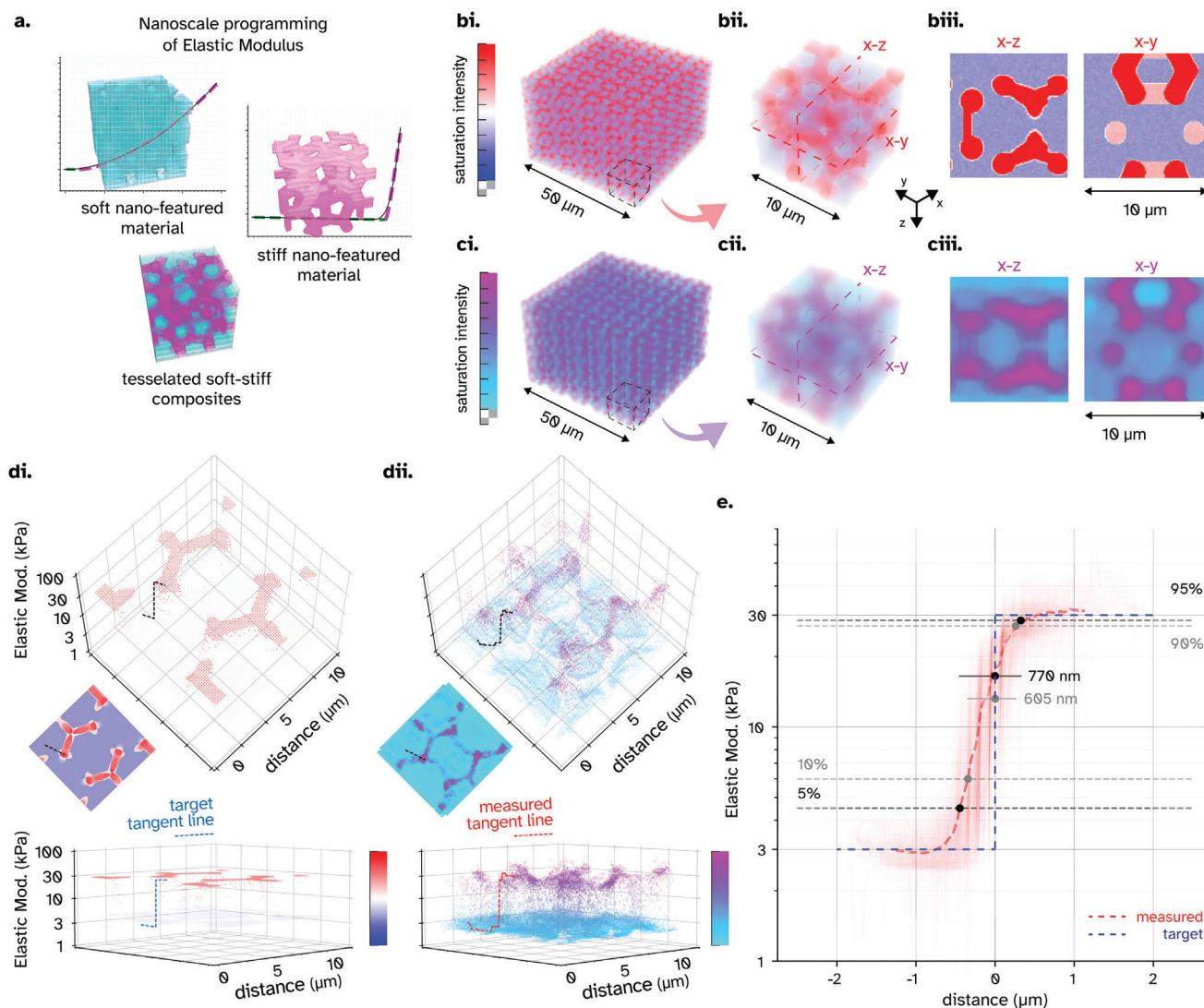


Figure 3. Materials with nanovoxelated elastic moduli. a) Materials with complex heteromechanics were demonstrated by programming voxels with a biphasic elastic modulus in a tessellated Weaire-Phelan lattice composite. A comparison between the b) 3D renders of target structure and c) 3D imaged structure, including (c (i)) the 50 μm super-structure, (c (ii)) a mean 10 μm unit cell, and (c (iii)) x-z and x-y planes through the structure. d) shows AFM force spectroscopy mapping of elastic modulus, comparing (d (i)) Target structure showing predicted elastic modulus distribution, (d (ii)) Measured elastic modulus distribution confirming the presence of heteromechanically tessellated soft-stiff structures. e) Quantification of spatial resolution of mechanical transition, showing elastic modulus along lines tangent to the soft-stiff interface. A transition length at the nanoscale is observed with a 5%–95% or 10%–90% transition in 770 and 605 nm, respectively.

to image the structures directly, with the denser, stiffer regions emitting stronger fluorescent signals under ultra-violet excitation (Weaire–Phelan – Figure 3c, gyroid, cubic, octet, Kelvin unit cells—Figures S12–S17, Supporting Information). This differential in fluorescence intensity facilitated the detailed rendering of the 3D structures of our printed materials, enabling a direct comparison between the imaged structures (Figure 3c) and their theoretical designs (Figure 3b), as well as confirming the hypothesized local differences to polymer density.

The local elastic moduli were measured using AFM force spectroscopy, mapping the surface of the unit cells (Weaire-Phelan Figure 3d, gyroid, cubic, octet, Kelvin unit cells – Figures S12–S17, Supporting Information). The results con-

firmed the presence of a monolithic composite material characterized by periodic unit cells with heteromechanically tessellated soft-stiff structures, mirroring the patterns observed in confocal microscopy. A comparison between the model (Figure 3d(i)) and measured structures (Figure 3d(ii)) is presented.

We next sought to quantify the spatial resolution of mechanical transition, analyzing the elastic modulus along lines tangent to the transition (Figure 3d). The mean transition length across all unit cells was then overlaid (Figure 3e), revealing a nanoscale transition length, with changes in elastic modulus over one order of magnitude occurring from 5% to 95% and from 10% to 90% between the programmed values of 3–30 kPa within a range of 770–605 nm, respectively. Comparing our

results with existing reports highlights the significant advancement our method represents. For instance, multimaterial direct ink writing has been utilized to print photocurable elastomeric foams with features ≈ 2.1 mm.^[29] Similarly, Stratasys Object500 Connex3^[30] and J750 printers,^[32] have produced materials with mm-scale features, yet the resolution details remain unspecified. Additionally, magnetically-assisted 3D printing also carries mm-scale feature limitations.^[33] More advanced techniques like multimaterial multinozzle 3D printing, achieve a 320 μm transition length between soft and stiff materials.^[24] Meanwhile, centrifugal multimaterial 3D printing offers a minimal transition of 100 μm between different plastic materials ranging from 0.8 MPa to 1 GPa.^[1] By contrast, our method achieves a transition length of 770 nm (Figure 3e), representing a 130-fold improvement in the precision of mechanical property modulation compared to the previous lowest value in the literature of 100 μm .^[1]

3. Conclusions

We present a method for fabricating materials designed with nanovoxelated elastic moduli. Our approach allows for the precise control of local mechanical properties at the nanoscale without compromising structural integrity, achieved through the development of a volume-conserving PEGDA copolymer photoresist and an open-source software platform, OpenScribe, which encourages collaborative advancements and customization across disciplines. Using our resist and software, we successfully generate materials with intricate periodic unit cells featuring heteromechanically tessellated soft-stiff structures in various lattice geometries. We fabricated materials with distinct elastic moduli regions, with transitions between soft and stiff regions as fine as 770 nm, representing a 130-fold improvement over existing methods,^[1,24] providing unprecedented control over the nanoscale mechanical properties of printed materials.

The finite size of the contact area between the AFM probe and the sample imposes a limit on the spatial resolution of elastic moduli measurements and therefore the length of the transition region. Calculations using Hertzian contact mechanics indicate that the contact radius ranges from ≈ 448 nm in stiffer regions to 965 nm in softer regions. This suggests that the observed mechanical transition width of 770 nm may represent an upper bound constrained by the probe's contact area, with the possibility of the actual mechanical transition being sharper than what our measurements can resolve. The alignment of our observed transition width with these theoretical limits underscores the robustness of our method and the precision of our fabrication approach (see [Supporting Information](#) for an extended discussion on the measurement of elastic maps).

Our method's ability to voxelate elastic properties with nanoscale precision paves the way for the development of a new generation of materials with nanovoxelated properties that have been precisely designed. Such materials could be driven by extending our approach to voxelate other material properties such as electrical conductivity, biofunctionalities, thermal conductivity, optical refractivity, and magnetic permeability. For instance, voxelating electrical conductivity could lead to the creation of compact conductive pathways within materials, freeing printed circuit boards from their traditional 2D construction and en-

abling the next generation of 3D structured electronics, that can be scaled cubically, thereby enabling vast improvements to data storage and computation.^[43,44] Materials with high strength and toughness could be fabricated by replicating the multiscale hierarchical structures present in nature.^[19] Controlling thermal conductivity at the nanoscale could result in advanced thermal management systems for electronics and aerospace applications, where heat dissipation is critical. The integration of voxelated bio-functionalities, as demonstrated with our inclusion of laminin for specific cell attachment, highlights the potential for tailored interactions with biological systems, opening the potential for materials to program biological interactions.^[26] Finally, complex materials with programmable shape transformations could be realized through future computational frameworks that solve the inverse problem of mapping desired deformed shapes to specific moduli distributions.

In summary, our method sets a new limit for fabricating materials with controlled mechanical properties at the nanoscale, setting the stage for broader applications. By expanding the range of voxelated properties, we can create complex metamaterials with multifunctional capabilities, driving innovation in numerous fields and enabling new technologies that were previously unattainable.

4. Experimental Section

Photoresist: The photoresist developed for this work uses a copolymer hydrogel of poly(ethylene glycol) diacrylate average $M_n = 250$ g mol⁻¹ (PEGDA250), 475629-100ML (Sigma-Aldrich), poly(ethylene glycol) diacrylate average $M_n = 575$ g mol⁻¹ (PEGDA575), 437441-100ML (Sigma-Aldrich), the photoinitiator phenylbis(2,4,6-trimethylbenzoyl)phosphine oxide (BAPO), 511447-10G (Sigma-Aldrich), an enzymatic oxidase system composed of d-(+)-glucose (dextrose); powder, BioReagent, G7021-100G (Sigma-Aldrich), and glucose oxidase from aspergillus niger, G6125-250KU (Sigma-Aldrich), a cellulose thickener hydroxypropyl-methyl cellulose, viscosity 2600–5600 cP, H7509-100G (Sigma-Aldrich), with a dimethyl sulfoxide (DMSO) solvent, 472301-500ML (Sigma-Aldrich). The final volume conserving resist was mixed with glucose (3.8%), glucose oxidase (0.23%), cellulose (2%), PEGDA250 (10%), and PEGDA575 (30%). The reactions and repeatability of the experiments were found to be highly dependent on water contamination within the photoresist. Accordingly, all liquid reagents were stored in filtered (0.22 μm) in zeolite 3A molecular sieve.

Printing: 3DNP was completed with the Photonic Professional GT2, Nanoscribe, GmbH, with print instructions generated using OpenScribe – github.com/peterlionelnewman/openscribe. The GT2 device was equipped with a femtosecond fiber laser with the center wavelength at 780 nm, calibrated to a power of 50 mW (at NanoWrite setting 100%), and used in continuous pulsed mode. All prints were performed in DiLL (Dip-In Laser Lithography) mode, ensuring constant laser transmission path length throughout the fabrication process. All prints used the Carl Zeiss Plan-neofluar 25x NA0.8 objective. After printing, structures were washed in DMSO while on a plate shaker, removing and replenishing the DMSO 3 times. For measurement of swelling, printed structures were left on a plate shaker in MQ H₂O overnight, for at least 10 h, before confocal microscopy. The OpenScribe software interpolated optimal printing parameters from empirically determined relationships between laser power, hatch volume, and measured elastic moduli (characterized via AFM force spectroscopy, see Figure 2). For fabricating materials with distinct mechanical regions, these interpolated relationships determined that soft regions of 3 kPa required 31.5 mW laser power with a hatch volume of ≈ 0.15 μm^3 . Stiff regions of 30 kPa were printed using 55.5 mW laser power with a hatch volume of 0.0054 μm^3 (see Direct programming of object elastic modulus—in Table S2, Supporting Information for further details).

Cell Attachment Assay: The attachment assay inset in Figure 1 used hiPSCs – HPSI0314i-hoik_1 hiPSC line, obtained from the Wellcome Sanger Institute with the help of Cell Bank Australia. For routine passaging, cells were passaged with ReLeSR and grown on hESC-qualified Geltrex-coated 6-well plates. All experiments used Essential 8 Flex media (E8F). For attachment assay, cells were cultured over the photoresist supplemented with 50 $\mu\text{g mL}^{-1}$, rh-laminin-521 (Gibco A29249). hiPSC cells were dissociated with Versene and pipetted into a single-cell suspension with a CEPT cocktail before seeding. All cells tested negative for mycoplasma contamination. For hADSCs, routine PCR assay checks (LookOut Mycoplasma qPCR Detection Kit, MP0040A-1KT) were completed for mycoplasma contamination, for hiPSC mycoplasma was tested using the fluorescent kit, MycoAlert™ Mycoplasma Detection Kit, Catalog #: LT07-318.

3D Imaging: Confocal microscopy was completed on a Zeiss LSM 800 Confocal microscope using 63×Objective Plan-Apochromat 63×/1.40NA Oil objective (with an in-plane lateral resolution of 0.413–0.124 μm per pixel) and pinhole diameter of 1.0 AU and azimuthal resolution of 0.4 μm . The 3D imaging was completed using a tiled image mosaic (raw data slice from 3D confocal in Figure S10, Supporting Information). Tiles were processed into semi-transparent 3D renders throughout this work (visualized with the VTK imaging toolkit—see OpenScribe software) following alignment, stitching, and illumination correction of an overlapping tile mosaic.

AFM Force Spectroscopy: AFM force spectroscopy was performed using the force mapping feature on an MFP-3D (Asylum, Santa Clara, CA) with Loctite AA350 – ultra-violet curable glue, AIO-TL-10 – all in one tipless AFM probes, 72986-5ML-F – 10 μm PS beads, manufactured in accordance with the protocol outlined in Norman et al.^[45] Indentation was completed to a force of 1 nN, with Elastic moduli calculated using a neo-hookean Ogden Hertz-fit model from force curves using the code – github.com/peterlionelnewman/force_spectroscopy. Data for force spectroscopic curves of AFM tip displacement against indentation force were rejected when discontinuities in the curves were present, corresponding to samples slipping and an inaccurate indentation. All force curves for mapping the print conditions to the elastic modulus were completed 16 times over a 20 μm^2 area in triplicate. Force maps showing heteromechanics were completed in quadruplicate, sampling 6400 locations over a 10 μm^2 grid, with 4 force curves sampled at each location (Figures S12–S17, Supporting Information). Tangent lines were calculated by first identifying boundaries between soft and stiff regions. Boundaries were calculated by Canny edge detection on theoretical elastography of regions of either 3 or 30 kPa. Each pixel of the map represented the 6400 locations that were probed during AFM force spectroscopy. A tangent line to the boundary was then calculated by finding the derivative of the polynomial fit of the boundary line. The elastic modulus was then extracted along the tangent line and overlaid into a single graph combining aligned tangent lines from all unit cells. Tangent lines that did not contain values both below 6 kPa and above 27 kPa were rejected from further calculation. The transition length was then calculated from the mean of the tangent lines by calculating the intersection at 5%–95% and 10%–90% points.

Supporting Information

Supporting Information is available from the Wiley Online Library or from the author.

Acknowledgements

The authors would like to thank Anthony Katselas and Chiara Neto for the generous use of AFM, and Vijay Bahtia and the Australian Centre for Microscopy and Microanalysis (ACMM) at the University of Sydney for the use of their equipment. P.N., I.R., and H.Z. acknowledge ARC LEIF grant funding LE210100156 for support of the Nanoscribe equipment. Additionally, the authors appreciate the discussions and idea exchanges with Ella Lambert, Queenie Yip, and Peter Maschmeyer. C.B.-K. acknowledges funding by the Deutsche Forschungsgemeinschaft (DFG, German Research Foundation) under Germany's Excellence Strategy for the Excellence Cluster "3D Matter Made to Order" (EXC–2082/1 – 390761711). The authors

acknowledge the facilities as well as the scientific and technical assistance of the Research and Prototype Foundry Core Research Facility at the University of Sydney, part of the NSW node of the NCRIS-enabled Australian National Fabrication Facility.

Open Access publishing facilitated by University of New South Wales, as part of the Wiley - University of New South Wales agreement via the Council of Australian University Librarians.

Conflict of Interest

The authors declare no conflict of interest.

Author Contributions

P.H.L.N. led the project, performed experimental work and analysis, and wrote the manuscript. S.C.G. and C.B.-K. provided input on optimizing the photochemical system. M.M. and I.R., assisted in authoring the paper. M.B., C.B.-K., and H.Z. contributed to revising the manuscript and to supervising the study.

Data Availability Statement

The data that support the findings of this study are available in the supplementary material of this article.

Keywords

3d printing, architected materials, elastic modulus, metamaterials, nanoscale materials

Received: October 23, 2024

Revised: January 29, 2025

Published online: March 6, 2025

- [1] J. Cheng, R. Wang, Z. Sun, Q. Liu, X. He, H. Li, H. Ye, X. Yang, X. Wei, Z. Li, B. Jian, W. Deng, Q. Ge, *Nat. Commun.* **2022**, *13*, 7931.
- [2] C. L. Bacquet, H. Al Ba'ba'a, M. J. Frazier, M. Nouh, M. I. Hussein, in *Advances in Applied Mechanics* (Ed.: M. I. Hussein), Elsevier, Amsterdam, Netherlands **2018**, 115–164.
- [3] Y. Tian, Y. Shen, *J. Sound Vib.* **2020**, *485*, 115566.
- [4] H. Van Swygenhoven, P. M. Derlet, A. G. Frøseth, *Nat. Mater.* **2004**, *3*, 399.
- [5] D. Jang, J. R. Greer, *Nat. Mater.* **2010**, *9*, 215.
- [6] T. Bückmann, M. Thiel, M. Kadic, R. Schittny, M. Wegener, *Nat. Commun.* **2014**, *5*, 4130.
- [7] B. Florijn, C. Coulais, M. van Hecke, *Phys. Rev. Lett.* **2014**, *113*, 175503.
- [8] S. Adhikari, T. Mukhopadhyay, A. Shaw, N. P. Lavery, *Int. J. Eng. Sci.* **2020**, *150*, 103231.
- [9] R. Lakes, *Science* **1987**, *235*, 1038.
- [10] Y.-C. Cheng, H.-C. Lu, X. Lee, H. Zeng, A. Priimagi, *Adv. Mater.* **2020**, *32*, 1906233.
- [11] M. Schaffner, J. A. Faber, L. Pianegonda, P. A. Rühls, F. Coulter, A. R. Studart, *Nat. Commun.* **2018**, *9*, 878.
- [12] K. K. Dudek, J. A. I. Martínez, G. Ulliac, M. Kadic, *Adv. Mater.* **2022**, *34*, 2110115.
- [13] Y. Chen, L. Jin, *Extreme Mech. Lett.* **2018**, *23*, 55.
- [14] T. Chen, M. Pauly, P. M. Reis, *Nature* **2021**, *589*, 386.
- [15] U. Waheed, C. W. Myant, S. N. Dobson, *Extreme Mech. Lett.* **2020**, *40*, 100865.

- [16] U. G. K. Wegst, H. Bai, E. Saiz, A. P. Tomsia, R. O. Ritchie, *Nat. Mater.* **2015**, *14*, 23.
- [17] H. Gao, B. Ji, I. L. Jäger, E. Arzt, P. Fratzl, *Proc. Natl. Acad. Sci.* **2003**, *100*, 5597.
- [18] M. Mirkhalaf, A. K. Dastjerdi, F. Barthelat, *Nat. Commun.* **2014**, *5*, 3166.
- [19] E. Munch, M. E. Launey, D. H. Alsem, E. Saiz, A. P. Tomsia, R. O. Ritchie, *Science* **2008**, *322*, 1516.
- [20] U. G. K. Wegst, M. F. Ashby, *Philos. Mag.* **2004**, *84*, 2167.
- [21] J. Aizenberg, J. C. Weaver, M. S. Thanawala, V. C. Sundar, D. E. Morse, P. Fratzl, *Science* **2005**, *309*, 275.
- [22] N. Reznikov, M. Bilton, L. Lari, M. M. Stevens, R. Kröger, *Science* **2018**, *360*, eaao2189.
- [23] M. Deubel, G. von Freymann, M. Wegener, S. Pereira, K. Busch, C. M. Soukoulis, *Nat. Mater.* **2004**, *3*, 444.
- [24] M. A. Skylar-Scott, J. Mueller, C. W. Visser, J. A. Lewis, *Nature* **2019**, *575*, 330.
- [25] Q. Wang, J. A. Jackson, Q. Ge, J. B. Hopkins, C. M. Spadaccini, N. X. Fang, *Phys. Rev. Lett.* **2016**, *117*, 175901.
- [26] P. L. H. Newman, Q. Yip, P. Osteil, T. A. Anderson, J. Q. J. Sun, D. Kempe, M. Biro, J.-W. Shin, P. P. L. Tam, H. Zreiqat, *Adv. Sci.* **2023**, *10*, 2204741.
- [27] F. Mayer, S. Richter, J. Westhauser, E. Blasco, C. Barner-Kowollik, M. Wegener, *Sci. Adv.* **2019**, *5*, eaau9160.
- [28] T. J. Ober, D. Foresti, J. A. Lewis, *Proc. Natl. Acad. Sci.* **2015**, *112*, 12293.
- [29] O. D. Yirmibesoglu, L. E. Simonsen, R. Manson, J. Davidson, K. Healy, Y. Menguc, T. Wallin, *Commun. Mater.* **2021**, *2*, 82.
- [30] M. J. Mirzaali, H. Pahlavani, E. Yarali, A. A. Zadpoor, *Sci. Rep.* **2020**, *10*, 11488.
- [31] D. Chen, X. Zheng, *Sci. Rep.* **2018**, *8*, 9139.
- [32] A. Ghimire, P.-Y. Chen, *Mater. Des.* **2024**, *238*, 112677.
- [33] D. Kokkinis, M. Schaffner, A. R. Studart, *Nat. Commun.* **2015**, *6*, 8643.
- [34] M. Hippler, E. Blasco, J. Qu, M. Tanaka, C. Barner-Kowollik, M. Wegener, M. Bastmeyer, *Nat. Commun.* **2019**, *10*, 232.
- [35] Y. Guo, J. Zhang, W. Hu, M. T. A. Khan, M. Sitti, *Nat. Commun.* **2021**, *12*, 5936.
- [36] Q. Ji, J. Moughames, X. Chen, G. Fang, J. J. Huaroto, V. Laude, J. A. I. Martínez, G. Ulliac, C. Clévy, P. Lutz, K. Rabenoroosa, V. Guelpa, A. Spangenberg, J. Liang, A. Mosset, M. Kadic, *Commun. Mater.* **2021**, *2*, 93.
- [37] P. Kiefer, V. Hahn, M. Nardi, L. Yang, E. Blasco, C. Barner-Kowollik, M. Wegener, *Adv. Opt. Mater.* **2020**, *8*, 2000895.
- [38] A. Sydney Gladman, E. A. Matsumoto, R. G. Nuzzo, L. Mahadevan, J. A. Lewis, *Nat. Mater.* **2016**, *15*, 413.
- [39] J. R. Tumbleston, D. Shirvanyants, N. Ermoshkin, R. Januszewicz, A. R. Johnson, D. Kelly, K. Chen, R. Pinschmidt, J. P. Rolland, A. Ermoshkin, E. T. Samulski, J. M. DeSimone, *Science* **2015**, *347*, 1349.
- [40] J. C. Grim, T. E. Brown, B. A. Aguado, D. A. Chapnick, A. L. Viert, X. Liu, K. S. Anseth, *ACS Cent. Sci.* **2018**, *4*, 909.
- [41] B. Trappmann, B. M. Baker, W. J. Polacheck, C. K. Choi, J. A. Burdick, C. S. Chen, *Nat. Commun.* **2017**, *8*, 371.
- [42] T. Frenzel, M. Kadic, M. Wegener, *Science* **2017**, *358*, 1072.
- [43] L. G. Wright, T. Onodera, M. M. Stein, T. Wang, D. T. Schachter, Z. Hu, P. L. McMahon, *Nature* **2022**, *601*, 549.
- [44] X. Xia, C. M. Spadaccini, J. R. Greer, *Nat. Rev. Mater.* **2022**, *7*, 683.
- [45] M. D. Norman, S. A. Ferreira, G. M. Jowett, L. Bozec, E. Gentleman, *Nat. Protoc.* **2021**, *16*, 2418.